J. Fluid Mech. (2009), *vol.* 631, *pp.* 1–21. © 2009 Cambridge University Press
doi:10.1017/S0022112009005837 Printed in the United Kingdom

Pressure-driven flow in a two-dimensional channel with porous walls

QUAN ZHANG[1] AND ANDREA PROSPERETTI[1,2]†

[1] Department of Mechanical Engineering, Johns Hopkins University, Baltimore, MD 21218, USA
[2] Faculty of Science & Technology and Burgerscentrum, University of Twente, AE 7500 Enschede, The Netherlands

(Received 14 May 2008 and in revised form 31 December 2008)

The finite-Reynolds-number two-dimensional flow in a channel bounded by a porous medium is studied numerically. The medium is modelled by aligned cylinders in a square or staggered arrangement. Detailed results on the flow structure and slip coefficient are reported. The hydrodynamic force and couple acting on the cylinder layer bounding the porous medium are also evaluated as a function of the Reynolds number. In particular, it is shown that, at finite Reynolds numbers, a lift force acts on the bodies, which may be significant for the mobilization of bottom sediments.

1. Introduction

Flow along the surface bounding a porous medium occurs in a variety of natural and engineering systems. Prime examples can be found in the environment: the bottom of rivers, lakes and oceans, atmospheric boundary layers over a forest canopy, overland flow of rain and irrigation waters and many others. A porous medium forms the boundary of wider flow passages e.g. in a cracked porous medium, of interest in situations as diverse as groundwater flow, oil extraction and geothermal engineering. Technological instances of such flows are also abundant: filtering, solid-bed catalysts, packed-bed heat exchangers and transpiration cooling to name a few.

Beavers & Joseph (1967) carried out experiments in an effectively two-dimensional channel bounded by a porous medium at $y=0$ and an impermeable wall at $y=H$ and introduced the notion of slip coefficient α defined by

$$\left.\frac{\mathrm{d}U}{\mathrm{d}y}\right|_{y=0^+} = \frac{\alpha}{\sqrt{\kappa}}\,(U_i - U_D) \tag{1.1}$$

where U_i is the 'slip velocity' at the interface $y=0$, U_D is the Darcy velocity and κ is the permeability of the porous medium. The last two quantities are related by

$$-\frac{\mathrm{d}p}{\mathrm{d}x} = \frac{\mu}{\kappa}U_D \tag{1.2}$$

in which μ is the fluid viscosity, $\mathrm{d}p/\mathrm{d}x$ the imposed pressure gradient, and the flow is assumed to take place in the x-direction. This well-known relation is valid in the low-Reynolds-number conditions characteristic of many porous media flows. By independently inferring U_i, U_D and κ from the measured flows in the porous medium and the channel, Beavers & Joseph (1967) determined α finding that

† Email address for correspondence: prosperetti@jhu.edu

'A slip-flow boundary condition with one experimentally determined parameter is not inconsistent with the experimental data'; typical values were in the range $\alpha \sim 0.1$–4.0.

Sahraoui & Kaviany (1992) attempted to determine α numerically on a two-dimensional model of a porous medium realized with an array of cylinders. In their work the volume (area) fraction β occupied by the solids ranged between 20 % and 50 %, but the thickness of the clear-fluid region was only a few times the cylinder radius, which caused their channel height to be comparable to the roughness of the effective porous medium interface thus somewhat obscuring the physical picture. An important aspect of their work is the inclusion of inertial effects, which become important near the porous medium interface as the Reynolds number increases.

The present work builds on that of Sahraoui & Kaviany: we use a similar two-dimensional model consisting of cylinders arranged in a square or staggered pattern and we investigate the details of the pressure-driven flow field at finite Reynolds number. Our most interesting result is the identification of a lift force acting on the bodies at the surface of the porous medium, which could prove of practical significance, e.g. in providing the initial impetus under which sand grains or pebbles become suspended in a flow.

In their study of fluid flow in a channel containing 300 cylinders, Choi & Joseph (2001) also found a lift force on the particles. They started the simulation from rest and allowed the particles to move finding that the bed inflates due to a 'pumping of liquid into [it] at the earliest times'. Ours is a steady-state simulation and there is no exchange of fluid between the bed and the clear space above it, although the lift force persists. This result suggests that the stress distribution over the particle surface is able by itself to generate a lift force even without flow in and out of the bed.

The studies of Sahraoui & Kaviany and Choi & Joseph are among the very few which deviate from the Stokes-flow assumption made by many authors, starting with Larson & Higdon (1986, 1987) who studied the shear flow through semi-infinite cylinder arrays using a boundary integral method. The most recent work of this type is the paper by James & Davis (2001) who used a singularity method to find an approximate solution for planar Couette and Poiseuille flow in a channel partially filled by a cross-stream array of cylinders occupying a relatively small (less than 10 %) area fraction. This work also contains an excellent review of previous studies.

A recent experimental study of the situation postulated in these theoretical works has been carried out by Tachie, James & Currie (2003) in a Taylor–Couette-like apparatus with a bank of two-dimensional cylinders of various cross-sections arranged parallel to the surface of the rotating wall and therefore oriented across the flow. They observed eddies in the fluid space near the outer cylinder rows which are qualitatively similar to the ones described below in § 4. The Reynolds number in this experiment was very small and no results with inertial effects were reported. Eddies in the top layer of a model porous medium made with randomly arranged spheres were also observed by Goharzadeh, Khalili & Jørgensen (2005) (see an enlargement of their figure 4). The same group carried out similar experiments with the flow over a 'brush-like' cylinder arrangement (Tachie, James & Currie 2004; Agelinchaab, Tachie & Ruth 2006), a situation rather different from the one considered here.

The related problem of flow in an infinite cylinder array has been tackled, among others, by Sangani & Acrivos (1982), Sangani & Yao (1988) and Sangani & Behl (1989). These studies were conducted in the Stokes-flow approximation. More recently Koch & Ladd (1997) and Hill, Koch & Ladd (2001) investigated inertial effects at moderate Reynolds number for cylinder and sphere arrangements.

While, according to (1.1), the velocity undergoes a discontinuity at the porous medium interface, other models lead to a continuous velocity profile. The most widespread one, and historically the most important, is based on the Brinkman (1947) equation which, again for two-dimensional flow in the x-direction, is

$$-\frac{\mathrm{d}p}{\mathrm{d}x} = \frac{\mu}{\kappa}U - \frac{\mathrm{d}}{\mathrm{d}y}\left(\mu_{eff}\frac{\mathrm{d}U}{\mathrm{d}y}\right). \tag{1.3}$$

In a uniform medium the y-derivatives vanish and U becomes the Darcy velocity (1.2). In Brinkman's original paper the effective viscosity was taken as the pure fluid viscosity. Several authors have questioned this assumption and have attempted to improve on it analytically (e.g. Adler, Mills & Quemada 1978; Koplik, Levine & Zee 1983) and numerically (e.g. Martys, Bentz & Garboczi 1994). An illuminating discussion of an extended version of the Brinkman model and its connection to the slip coefficient has recently been given by Le Bars & Worster (2006), who retained the assumption $\mu_{eff} = \mu$.

2. Slip conditions

The Beavers–Joseph condition (1.1) may be recast in terms of a partial slip condition by writing

$$U_i = \lambda \left.\frac{\mathrm{d}U}{\mathrm{d}y}\right|_{y=0^+}, \tag{2.1}$$

in which λ is the slip length. By comparing (1.1) to (2.1) we find the following relationship between α and λ:

$$\frac{1}{\alpha} = \frac{\lambda}{\sqrt{\kappa}}\left(1 - \frac{U_D}{U_i}\right). \tag{2.2}$$

If the flow in the channel is approximated as a Poiseuille flow with slip at the wall, one readily obtains, from (2.1),

$$\lambda = \frac{2\mu U_i}{H(-\mathrm{d}p/\mathrm{d}x)}. \tag{2.3}$$

It is useful to present the computational results in terms of characteristic scales. For velocity, an obvious scale is provided by the mean velocity in Poiseuille flow, i.e. the horizontal velocity averaged over the height H of the channel

$$U_m = \frac{H^2(-\mathrm{d}p/\mathrm{d}x)}{12\mu}. \tag{2.4}$$

This velocity scale is much greater than the interfacial velocity U_i of (1.1). To estimate the scale U_* for this latter quantity we note that, usually, $U_i \gg U_D$, and that the slip coefficient is a number of order 1. Equation (1.1) then suggests that $U_* \sim \sqrt{\kappa}\mathrm{d}U/\mathrm{d}y$. The velocity gradient can be estimated from the wall velocity gradient for parabolic flow which is given by

$$\left.\frac{\mathrm{d}U}{\mathrm{d}y}\right|_{y=0+} = \frac{H(-\mathrm{d}p/\mathrm{d}x)}{2\mu} \tag{2.5}$$

irrespective of the magnitude of the wall slip. With this argument we are led to

$$U_* = \frac{H(-\mathrm{d}p/\mathrm{d}x)\sqrt{\kappa}}{2\mu} \tag{2.6}$$

as the characteristic scale of the interface velocity U_i. With $U_D = \kappa(-\mathrm{d}p/\mathrm{d}x)/\mu$, we see that

$$\frac{U_D}{U_*} = \frac{2\sqrt{\kappa}}{H} \tag{2.7}$$

so that the assumption $U_D \ll U_*$ is consistent. The ratio of the two velocity scales is

$$\frac{U_*}{U_m} = \frac{6\sqrt{\kappa}}{H}, \tag{2.8}$$

which is a small number as expected.

The two velocities U_m and U_* permit us to define two Reynolds numbers

$$Re_H = \frac{HU_m}{\nu}, \quad Re = \frac{2aU_*}{\nu}, \tag{2.9}$$

where a is the cylinder radius and ν the kinematic viscosity; Re_H is useful to characterize the flow in the channel while Re is relevant for the flow near the surface of the porous medium. The ratio of these two Reynolds number is the small number $Re/Re_H = 12a\sqrt{\kappa}/H^2$.

We will show results for the force and couple on the cylinders in the top layer. For the former, an appropriate scale F_* is the shear stress at the interface, $\tau_w \simeq \mu\, \mathrm{d}U/\mathrm{d}y|_{y=0+}$ multiplied by the particle diameter, although this scale does not include the pressure contribution and might therefore somewhat underestimate the force. For the couple, the appropriate scale L_* is the scale for the force multiplied by the particle radius a. Thus, we set

$$F_* = -\frac{\mathrm{d}p}{\mathrm{d}x}\, aH, \quad L_* = -\frac{\mathrm{d}p}{\mathrm{d}x}\, a^2 H. \tag{2.10}$$

For a given arrangement of the cylinders, the independent dimensionless parameters of the calculation can taken to be

$$\beta, \quad \frac{H}{a}, \quad \frac{a^3(-\mathrm{d}p/\mathrm{d}x)}{\mu\nu}, \tag{2.11}$$

with β the volume (area) fraction of the solids. For a square array which, for given β, uniquely determines the permeability κ (see (3.3) and (3.4)), this quantity is related to the dimensionless particle spacing by $L/a = \sqrt{\pi/\beta}$. The channel and interfacial Reynolds numbers Re_H and Re are related to the dimensionless channel height, permeability and pressure gradient by

$$Re_H = \frac{1}{6}\left(\frac{H}{a}\right)^3 \frac{a^3(-\mathrm{d}p/\mathrm{d}x)}{\mu\nu}, \quad Re = \frac{H\sqrt{\kappa}}{a^2}\frac{a^3(-\mathrm{d}p/\mathrm{d}x)}{\mu\nu}. \tag{2.12}$$

3. Numerical method and validation

Our numerical simulations are carried out using the PHYSALIS method which is described in detail in Takagi *et al.* (2003) and Zhang & Prosperetti (2003, 2005). The method is based on the observation that, due to the no-slip condition, in the immediate neighbourhood of each particle the Navier–Stokes equations can be accurately approximated by the linearized Stokes equations whatever the Reynolds number is. As the Reynolds number increases, the region where this approximation is applicable shrinks, but is never zero. For bodies with a simple shape, such as cylinders, the Stokes solution can be expressed in analytic form as a superposition

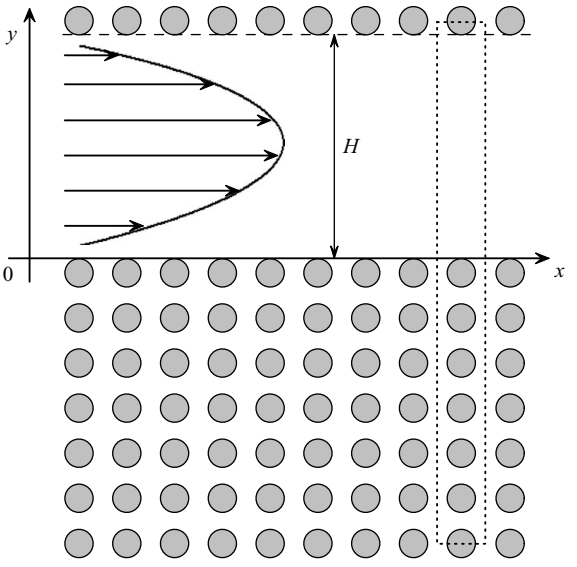

FIGURE 1. Illustration of the flow studied in this paper. The model porous medium consists of seven parallel cylinder rows in a square array, as here, or in a staggered configuration; periodicity in the vertical direction is assumed.

of modes containing undetermined coefficients, which are calculated by matching the local analytic solution with a finite-difference solution away from the particles. The latter is calculated by a standard first-order projection method. Some of the coefficients give the hydrodynamic force and couple on the bodies directly, avoiding the need to integrate the fluid stress over the body surface. Furthermore, the no-slip condition at the surface of the bodies is satisfied exactly. After some convergence tests, we found that four modes were sufficient for a good resolution of the flow. On the basis of earlier experience with this type of simulation, we used 16 cells per cylinder diameter. This resolution is adequate because the thickness of the Stokes region can be estimated to be of the order of $a/\sqrt{Re}$ (Zhang & Prosperetti 2003). Thus, 16 nodes per diameter are sufficient up to Re of order 50, which is well above the largest value attained by the interfacial Reynolds number in the present calculations.

The flow situation we consider is shown in figure 1. The system is periodic in the vertical direction with alternating layers of seven horizontal rows of cylinders and layers of clear fluid. By imposing periodicity conditions in the direction x of the mean flow, we can limit our consideration to a single vertical 'slice' of the flow containing a vertical line of seven cylinders. As shown later, the decay of the flow away from the surface of the porous medium is fast enough that this number is sufficient to simulate an effectively infinitely deep medium.

To test the accuracy of the calculation we carried out several comparisons with earlier work. Larson & Higdon (1987) simulated a simple-shear steady Stokes flow over a model porous medium consisting of many rows of aligned cylinders under a clear-fluid domain. The shear was generated by imposing a stress condition on the top boundary of their computational domain. To describe the same situation in our simulation, we replaced the periodicity conditions in the vertical direction by an imposed velocity on the top horizontal boundary of the clear-fluid domain and a zero velocity on a lower boundary placed close to the bottom

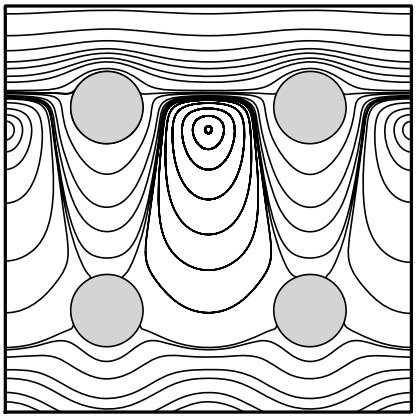

FIGURE 2. Calculated streamlines in the region of the two top cylinder rows for shear-induced flow at zero Reynolds number (square arrangement). This figure can be compared with figure 11(*c*) of Larson & Higdon (1987).

row of cylinders. The results were insensitive to the precise position of this lower boundary.

Figure 2 shows the streamlines in the region of the two top cylinder rows; the solids volume (area) fraction is 10 %. Comparison with the same situation computed by Larson & Higdon (1987) and shown in figure 11(*c*) of their paper is excellent. Both studies show the clear presence of recirculating eddies, quite unlike the results of James & Davis (2001) whose approximate method is evidently unable to deal with this relatively high concentration.

For an infinite periodic porous medium, a momentum balance over the fundamental cell relates the force F on the cylinder to the applied pressure gradient $-\mathrm{d}p/\mathrm{d}x$ according to

$$F = \frac{1}{n}\left(-\frac{\mathrm{d}p}{\mathrm{d}x}\right) = \frac{\pi a^2}{\beta}\left(-\frac{\mathrm{d}p}{\mathrm{d}x}\right), \tag{3.1}$$

in which n is the cylinder number density and $\beta = \pi a^2 n$ the solid volume (area) fraction. For moderate Reynolds numbers, Koch & Ladd (1997) showed that

$$\frac{F}{\mu\overline{U}} = k_0 + k_2 Re_d^2, \tag{3.2}$$

where $\overline{U}$ is the volume- (area-)averaged fluid velocity, $Re_d = 2a\rho\overline{U}/\mu$ and k_0, k_2 are functions of β; k_0 is related to the permeability κ by

$$k_0 = \frac{\pi a^2}{\beta\kappa} \tag{3.3}$$

and, for this quantity, Sangani & Acrivos (1982) showed that, for small β,

$$k_0 = \frac{4\pi}{\ln(\beta^{-1/2}) - 0.738 + \beta - 0.887\beta^2 + 2.038\beta^3 + O(\beta^4)} \tag{3.4}$$

while, for large β,

$$k_0 = \frac{9\pi}{2\sqrt{2}}\left(1 - \sqrt{\frac{4\beta}{\pi}}\right)^{-5/2} \tag{3.5}$$

	β	This work	Sangani & Acrivos (1982)	
Square array	15 %	36.21	36.16	Equation (17)
	30 %	102.94	102.90	Numerical
	45 %	327.04	343.21	Equation (18)
Staggered array	15 %	36.76	36.12	Equation (25)
	30 %	96.90	96.79	Numerical
	45 %	259.28	234.32	Equation (25)

TABLE 1. Values of k_0 from this work compared to those of Sangani & Acrivos (1982).

with the quantity in parentheses the dimensionless thickness of the gap between neighbouring cylinders. In addition to these asymptotic limits, Sangani & Acrivos (1982) calculated the permeability of infinite cylinder arrays at zero Reynolds number. Table 1 compares some of our results for k_0 with those of Sangani & Acrivos. Since they did not give results for $\beta = 45\,\%$, we were forced to use the approximate expression (3.5) which, as their figure 2 shows, is not quite accurate for this value of β. Nevertheless, the agreement between the two calculations is very good. To obtain these results, we calculated the permeability by using fully periodic boundary conditions on a fundamental cell containing only one body by the same procedure used by Koch & Ladd (1997).

We can use the results of Koch & Ladd (1997) to further validate our computations. To this end, we focus on the flow in the neighbourhood of the fourth row of cylinders. We verified that conditions here are close to those prevailing inside an infinite porous medium by comparing the velocity field and the drag force with the results obtained for a truly infinite porous medium realized as described before. The two simulations gave virtually identical results.

Figure 3 shows a graph of our computed dimensionless force (3.2) versus the mean Reynolds number Re_d plotted as a function of Re_d^2 for $\beta = 20\,\%$. These results are for an infinite porous medium and are to be compared with those shown in figure 1 of Koch & Ladd (1997). The values of k_0 and k_2 quoted by these authors are 51.19 and 0.065, to be compared with ours which are 51.545 and 0.065; Sangani & Acrivos (1982) quote $k_0 = 51.53$.

We define the average horizontal velocity at a depth y in the porous medium by

$$U(y) = \frac{1}{L}\int_{-L/2}^{L/2} u(x, y)\,\mathrm{d}x, \tag{3.6}$$

where, for the square array, L is the distance between the centres of two adjacent cylinders. To prove that our seven-cylinder thick layer is effectively equivalent to an infinite porous medium, we show in figure 4 a comparison between this average velocity in the region between the third and the fifth row of cylinders (symbols) with the corresponding results for an infinite porous medium (lines) for different dimensionless pressure gradients $a^3(-\mathrm{d}p/\mathrm{d}x)/(\mu v) = 0.24$, 0.48, 0.96 and 1.44 in ascending order, and for two channel widths, $H/a = 13.7$ and 17.1. The corresponding channel Reynolds numbers for $H/a = 13.7$ are $Re_H = 52$, 103, 205 and 308 while, for $H/a = 17.1$, $Re_H = 100$, 200, 400 and 600.

A similar graph for the region between the planes where the centres of the first and second cylinder rows are located is shown in figure 5. Only a slight asymmetry

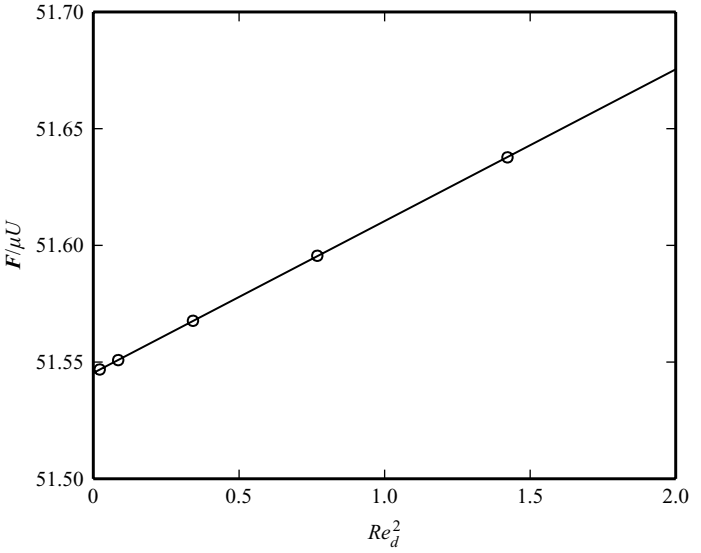

FIGURE 3. The force per unit length on a cylinder at different Reynolds numbers (circles) for an infinite porous medium compared with the fit (3.2) (solid line) for an area fraction $\beta = 20\,\%$ (square arrangement). Our calculated k_0 and k_2 are 51.545 and 0.065, to be compared with the values of Koch & Ladd (1997), which are 51.19 and 0.065.

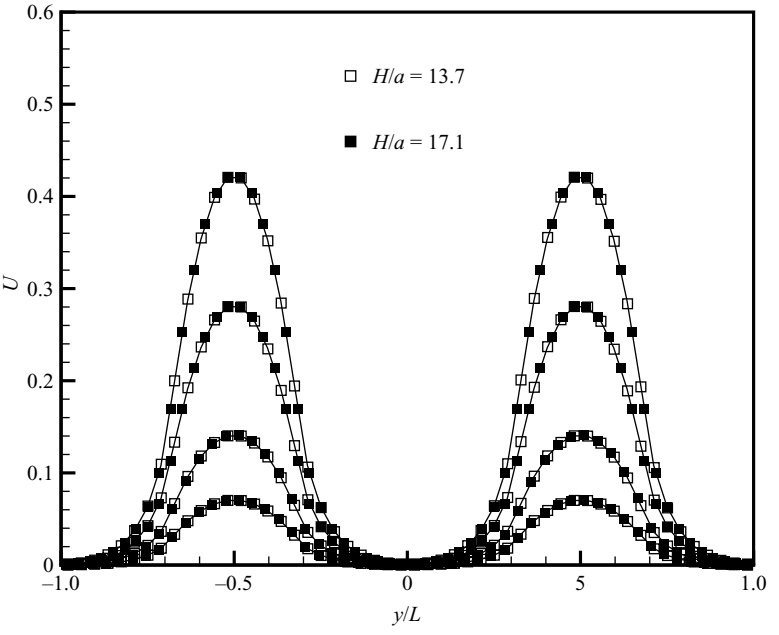

FIGURE 4. Comparison between the averaged velocity (3.6) inside an infinite porous medium (lines) and that in the region between the third and fifth rows of cylinders for two channels heights (symbols). The dimensionless pressure gradients are, in ascending order, $a^3(-\mathrm{d}p/\mathrm{d}x)/(\mu\nu) = 0.24$, 0.48, 0.96 and 1.44. The area fraction is $\beta = 30\,\%$ and the bodies are in the square arrangement; the y origin is set at the centreline of the fourth cylinder row.

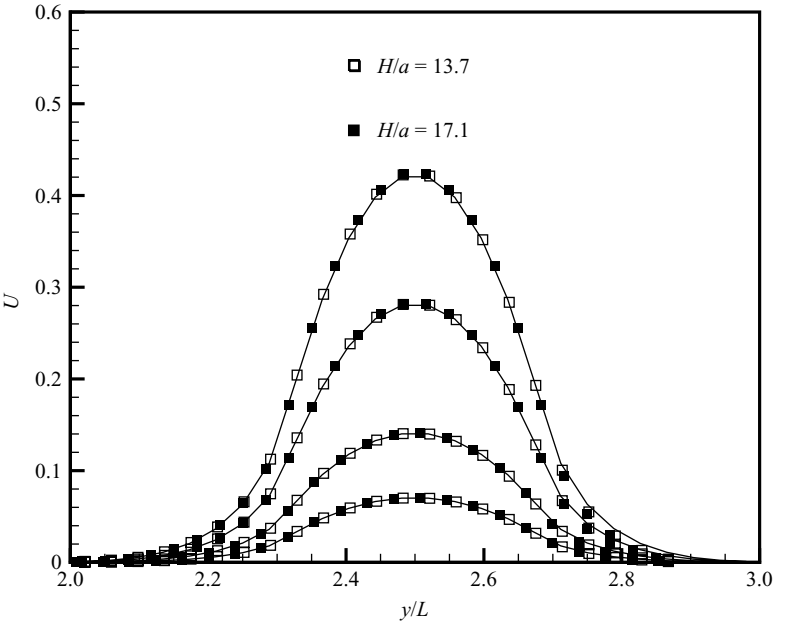

FIGURE 5. Comparison between the averaged velocity (3.6) inside an infinite porous medium (lines) and that in the region between the first and second row of cylinders for two channels heights (symbols). The dimensionless pressure gradients are, in ascending order, $a^3(-\mathrm{d}p/\mathrm{d}x)/(\mu v) = 0.24$, 0.48, 0.96 and 1.44. The area fraction is $\beta = 30\,\%$ and the bodies are in the square arrangement; the y origin is set on the mid-plane between the first and second cylinder row; $y/L = 3$ is the centre plane of the first cylinder row.

near the centre plane of the first row of cylinders is visible in the right corner of the figure, as put into evidence by the fact that, here, the points are slightly below the lines (which give the results for an infinite porous medium). This is the region where the recirculating eddies described later are mostly localized. In Sahraoui & Kaviany's work (Sahraoui & Kaviany 1992) an infinite-porous medium velocity boundary condition was imposed at the midplane between the first and the second cylinder row, i.e. $y/L = 2.5$ in this figure. While, on the basis of this figure, this may be a reasonable approximation, it might affect the small eddies, which are not shown in their paper.

4. Results

We now show typical results of the computations, starting with the flow field, turning then to the question of the slip at the interface and concluding with the force and couple on the particles. Most of the results are for the square array, but some examples for the staggered array will also be shown.

4.1. *Flow fields*

Figure 6 shows the streamlines in the region occupied by the upper four cylinder rows for $\beta = 15\,\%$ and different Reynolds numbers for the square array. In the upper row of bodies, for zero Reynolds number, the flow pattern is very similar to that shown in figure 7(a) of Pozrikidis (2001) for the flow over a single layer of cylinders in an infinite fluid. In his case, the flow under the cylinder layer was driven exclusively by the shear imposed above it, while in ours there is also a weak flow due to the imposed

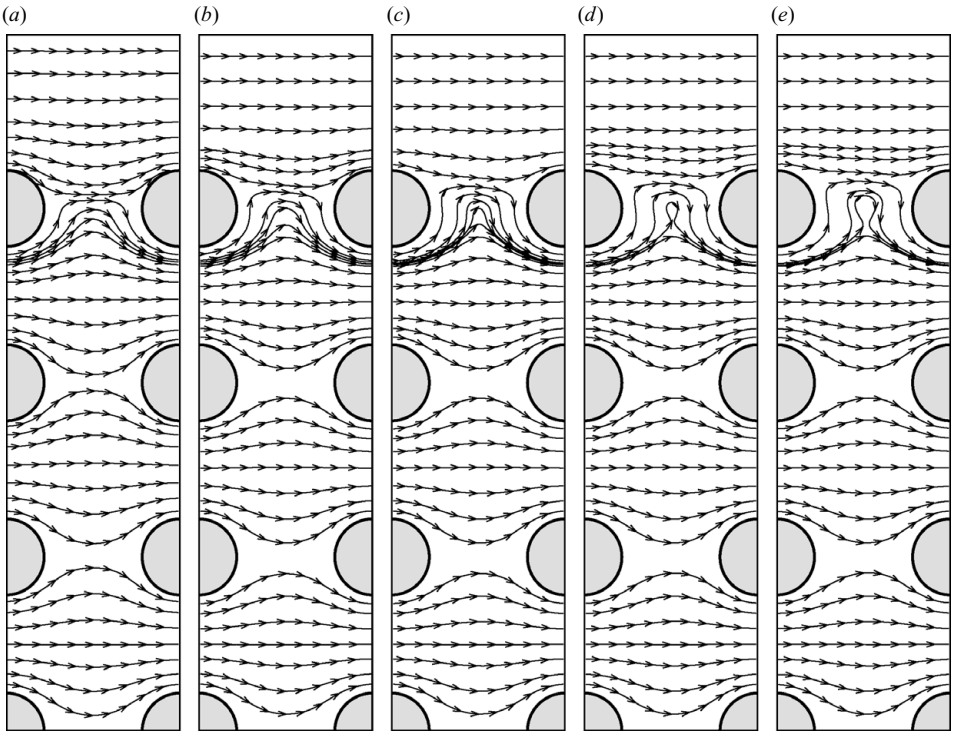

FIGURE 6. Streamlines for square arrays with cylinder area fraction $\beta = 15\,\%$ and channel width $H/a = 13.7$ at different Reynolds numbers: (*a*) $Re = 0, Re_H = 0$; (*b*) $Re = 5.00$, $Re_H = 103$; (*c*) $Re = 10.0\,, Re_H = 205$; (*d*) $Re = 15.0\,, Re_H = 308$; and (*e*) $Re = 20.4$, $Re_H = 420$.

pressure gradient. Since the velocity of this flow is small, its effect on the qualitative appearance of the streamlines is negligible. Pozrikidis himself noticed the similarity with the flow over a slit opened in a no-slip plane studied by Smith (1987).

A characteristic feature of the flow is the presence of a stagnation streamline connecting two horizontally adjacent cylinders in the topmost row. As Re increases, so does the horizontal velocity under this stagnation streamline, which forces more fluid to ascend and descend in the gap between the cylinders. These counter-directed streams in a narrow space give rise to an increasingly large dissipation which is eventually reduced by the formation of a slow recirculating eddy and the appearance of a second stagnation streamline connecting the lower sides of the cylinders. This process is not quite completed at the maximum Reynolds number shown in figure 6 and will be more evident in the examples shown later.

Inertia effects start being visible especially in the last two panels with the displacement of the flow pattern in the flow direction. A comparison between the streamlines under the second and third cylinder layers reveals negligible differences, which indicates that the flow in this region is already essentially the same as in an infinite porous medium.

Similar simulations for a narrower channel (smaller H), but the same interfacial Reynolds number Re defined in (2.9), show a less pronounced tendency to the 'pinching' of the streamlines and a delayed appearance of the recirculating eddy. These results can be explained from (2.8): constant Re means constant U_* and, if H is

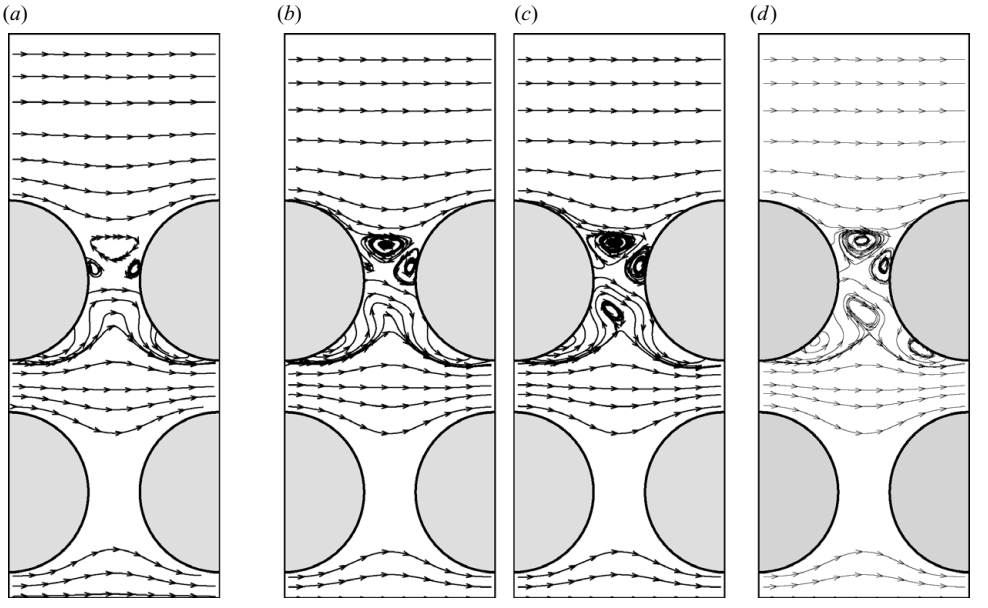

FIGURE 7. Streamlines for square arrays with cylinder area fraction $\beta = 45\,\%$ and channel width $H/a = 13.7$ at different Reynolds numbers: (*a*) $Re = 0$, $Re_H = 0$; (*b*) $Re = 0.961$, $Re_H = 103$; (*c*) $Re = 1.92$, $Re_H = 205$; and (*d*) $Re = 3.93$, $Re_H = 420$.

decreased, so is U_m. The slower flow in the channel (due to the greater flow resistance caused by the smaller height) causes a correspondingly weaker velocity above the stagnation streamline.

Figure 7 shows similar plots for $\beta = 45\,\%$, except that only the region above the centre plane of the second row of cylinders is shown as the flow deeper in the porous medium is very similar to the one shown in figure 6. Now a stagnation streamline on the lower side of the cylinders is present already at $Re = 0$, as are other stagnation and closed streamlines in the gap. The general appearance is reminiscent of the slow flow in a lid-driven cavity (see e.g. Shen & Floryan 1985; Hou *et al.* 1995; Patil, Lakshmisha & Rogg 2006) with the role of the lid played by the stagnation streamlines connecting the adjacent cylinders.

Two examples of the same flow in a wider channel ($H/a = 17.09$ in place of 13.69) are shown in figures 8(*a*) and 8(*b*). The interface velocity is larger here due to the increased channel width and the flow pattern in the gap fragments even further.

Figures 8(*c*) and 8(*d*) represent the streamlines for an intermediate volume fraction case, $\beta = 30\,\%$. The narrower inter-cylinder gap in comparison with the $\beta = 15\,\%$ case of figure 6 causes an earlier 'pinching' of the flow with a consequent appearance of a recirculating eddy.

Figure 9 shows examples of the flow for a staggered cylinder arrangement for volume fraction of 15 % (figure 9*a*,*b*) and 45 %. Qualitatively, the features of the flow are very similar to the ones seen in the previous examples.

Figure 10 shows examples of the pressure field. Darkness of the grey scale decreases with increasing magnitude of the dimensionless pressure $(p - \overline{p})/a(-\mathrm{d}p/\mathrm{d}x)$, in which $\overline{p}$ is the mean pressure over the entire flow field. Figures 10(*a*) and 10(*b*) are for the square array and figures 10(*c*) and 10(*d*) for the staggered array at two area fractions. Figures 10(*a*) and 10(*b*) are for area fractions of 15 %. It is seen that, in all

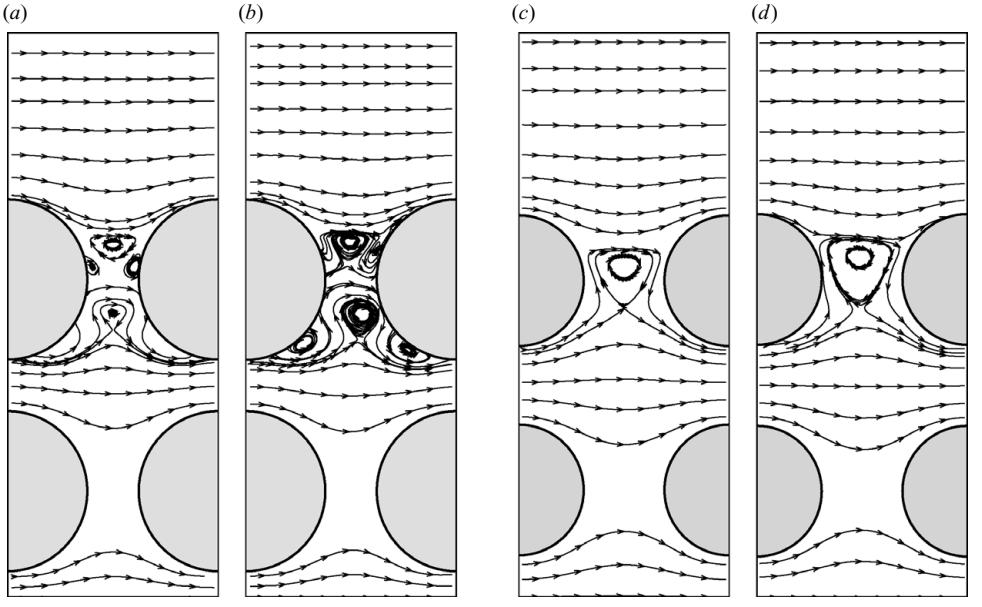

FIGURE 8. Streamlines for square arrays with cylinder area fraction $\beta = 45\,\%$ (a) and (b) and $30\,\%$ (c) and (d) and channel width $H/a = 17.1$ at different Reynolds numbers: (a) $Re = 0$, $Re_H = 0$; (b) $Re = 2.40$, $Re_H = 400$; (c) $Re = 0$, $Re_H = 0$; and (d) $Re = 5.23$, $Re_H = 400$.

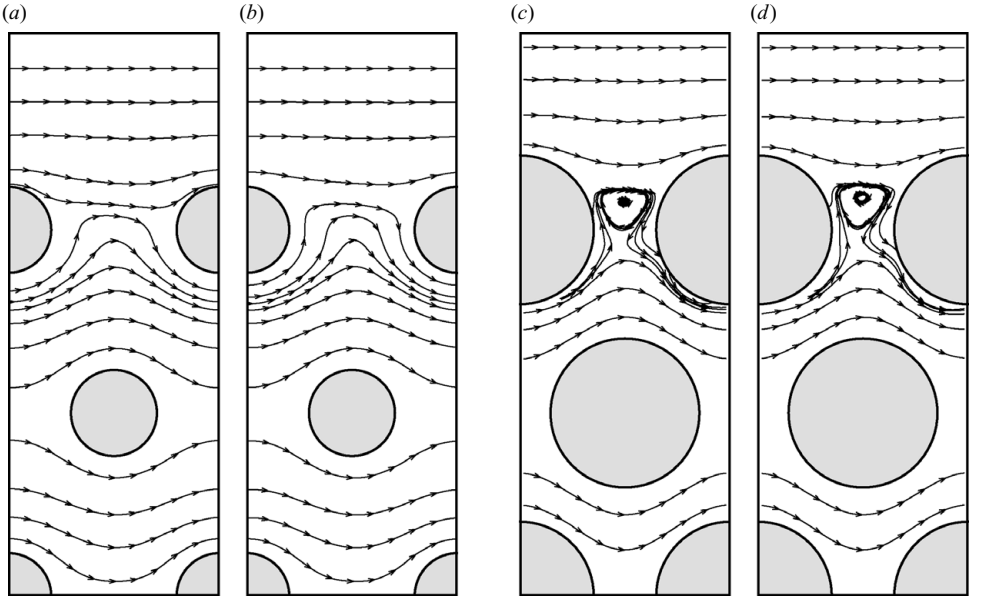

FIGURE 9. Streamlines for staggered arrays with cylinder area fraction $15\,\%$ (a) and (b) and $\beta = 45\,\%$ (c) and (d) and channel width $H/a = 13.7$ at different Reynolds numbers: (a) $Re = 4.96$, $Re_H = 103$; (b) $Re = 9.92$, $Re_H = 205$; (c) $Re = 1.08$, $Re_H = 103$; and (d) $Re = 3.24$, $Re_H = 308$.

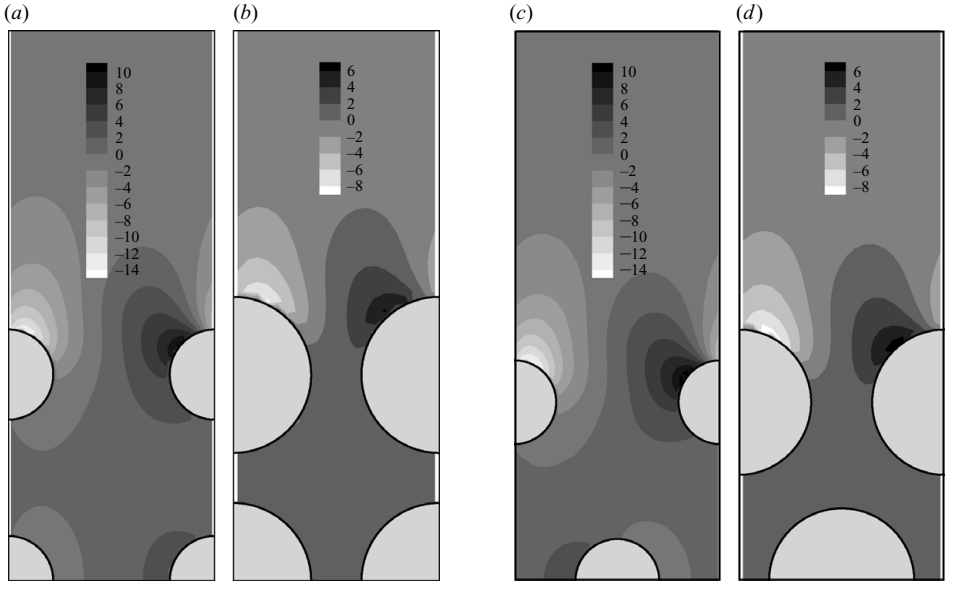

FIGURE 10. Pressure distribution in the region of the top two cylinder rows for the square (*a*) and (*b*) and staggered arrangements; (*a*) and (*c*) are for an area fraction of 15 % with $Re_H = 205$ and (*b*) and (*d*) for 45 % and $Re_H = 308$. The interfacial Reynolds numbers, from (*a*) to (*d*), are $Re = 10.0$, 2.88, 9.92, 3.24, respectively. The channel height is $H/a = 13.7$. Degree of darkness decreases with increasing magnitude.

cases, a marked pressure maximum forms near the attachment point of the stagnation streamline on the lee cylinder, and a pressure minimum near the separation point on the upstream cylinder. This feature has a significant effect on the lift force as will be seen later.

Between the bodies, for the square array, the iso-pressure lines are approximately perpendicular to the flow, but less so for the staggered array, which is responsible for the less symmetric eddies in the latter as compared to the former (cf. figures 7 and 9).

4.2. *Effective slip*

For the reasons explained by Sahraoui & Kaviany (1992) and James & Davis (2001), the interface is chosen to be the tangent plane to the cylinders facing the open channel. We define the interface velocity U_i, introduced in (1.1) of § 1, as the mean velocity (3.6) evaluated on this plane.

Figure 11 shows a typical profile of $U(y)$ defined in (3.6) (solid line) and compares it with a parabolic Poiseuille velocity distribution with the calculated U_i at $y = 0$ (dotted line) for $\beta = 15\,\%$ and $Re_H = 308$. The two results are nearly indistinguishable, which implies that the mean shear rate at the interface is well estimated by (2.5).

The non-dimensional quantity $U_i/U_* = \lambda/\sqrt{\kappa}$ is referred to as dimensionless slip velocity by James & Davis (2001) and Tachie *et al.* (2003). Graphs of U_i/U_* for $Re = 0$ and $\beta = 15\,\%$, 30 % and 45 % are shown in figure 12 as a function of the normalized inverse channel width a/H; the lines are quadratic fits to the calculated points and the corresponding numerical values are given in table 2. We use these fits to extrapolate the results to an infinite channel width, $a/H \to 0$, which, according to the considerations of James & Davis (2001), should permit one to calculate the slip coefficient α corresponding to linear shear flow. If, as these authors argue, α was the same for pressure-driven and shear-driven flow, for which $U_D = 0$, one would have

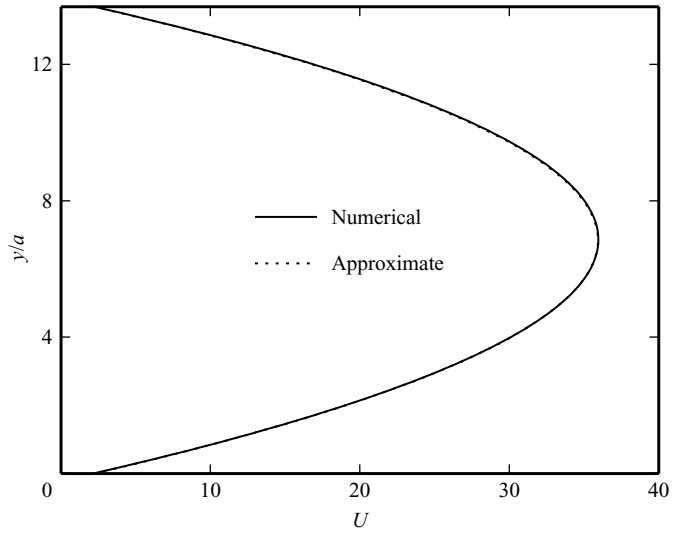

FIGURE 11. Dimensionless averaged velocity $a\overline{U}/\nu$ in the channel for cylinder area fraction $\beta = 15\,\%$, $H/a = 13.7$, $Re_H = 308$ (square array). The solid line is the numerical result and the dotted line is the analytical Poiseuille solution satisfying $U = U_i$ at $y = 0$, with the numerically computed U_i; the dimensionless value for this quantity is $aU_i/\nu = 2.19$.

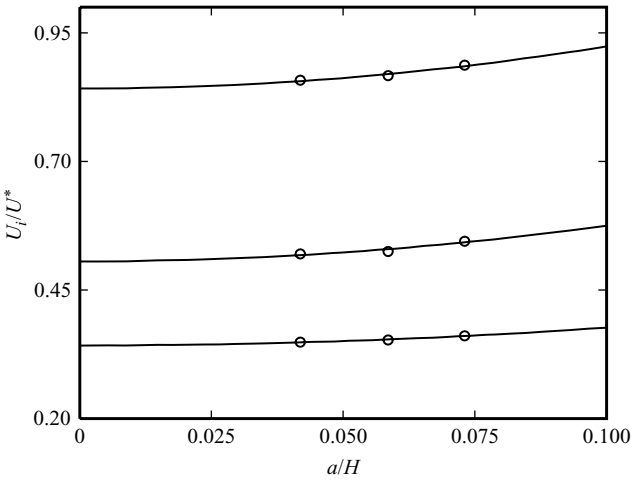

FIGURE 12. Dimensionless interfacial velocity for zero Reynolds number and different channel heights. The curves are quadratic fits.

from (2.2)

$$\frac{1}{\alpha} = \left(\frac{U_i}{U_*}\right)_{shear} = \left(\frac{U_i}{U_*}\right)_{press.} - \frac{U_D}{U_*} = \left(\frac{U_i}{U_*}\right)_{press.} - \frac{2\sqrt{\kappa}}{H} \tag{4.1}$$

where (2.7) has been used in the last step. For $\beta = 10\,\%$ and $16\,\%$ Tachie *et al.* (2003) measured a value 0.235 for shear-driven flow, which is close to the values 0.230–0.239 reported by James & Davis (2001) for $\beta = 10\,\%$. For $\beta = 15\,\%$ and the widest channel we have simulated, $H/a = 23.9$, our numerical result for the first term in the right-hand side is 0.349 while the last term has the value $U_D/U_* = 0.064$, with a

		β		
a/H	H/a	15 %	30 %	45 %
0	∞	0.3422	0.5057	0.8418
0.0419	23.87	0.3488	0.5202	0.8578
0.0585	17.1	0.3532	0.5251	0.8667
0.0730	13.7	0.3612	0.5448	0.8869

TABLE 2. Values of dimensionless slip velocity U_i/U_* defined in (4.2) for $Re = 0$.

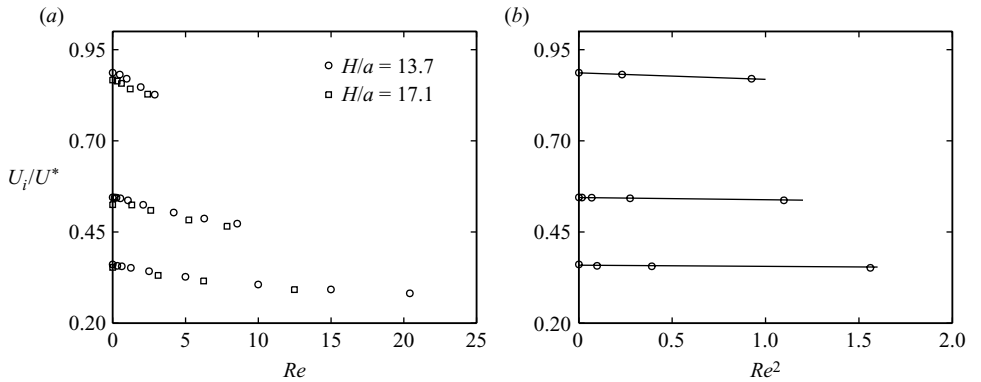

FIGURE 13. Dimensionless interfacial velocity as a function of the interfacial Reynolds number (2.9) for $\beta = 15\,\%$, 30 % and 45 % in ascending order. (*b*) An enlargement of the small-Re data of (*a*) plotted as function of Re^2, rather than Re, as suggested by (4.7).

net result $1/\alpha = 0.285$. Since, on the basis of the comparisons in § 3, our results appear to be accurate, this difference must be attributed to a small, but non-zero intrinsic difference between the slip features of pressure-driven and shear-driven flows. Thus, it appears that the Beavers–Joseph condition (1.1) is not universal, in the sense that the slip coefficient depends somewhat on the type of flow.

As found by Sahraoui & Kaviany (1992) for $Re = 0.1$ (see their figure 5*a*), increasing the channel width decreases the interface velocity which, once again, can be understood on the basis of (2.8): a wider channel offers less resistance to the flow, which decreases the fraction of fluid forced to flow in the porous medium and, with it, the interface velocity. This trend is also consistent with the results shown in figures 8 and 9 of James & Davis (2001).

Results for $U_i/U_* = \lambda/\sqrt{\kappa}$ at non-zero Reynolds number are shown for two channel widths in figure 13(*a*), with a detail for small Re in figure 13(*b*). At the larger channel Reynolds numbers, a boundary layer tends to form near the exposed solid surfaces which becomes more and more difficult to resolve with our grid. Hence we only present results up to a channel Reynolds number $Re_H = 420$. For the same channel Reynolds number, the interface Reynolds number decreases with increasing volume fraction due to the decrease of κ, which explains the unequal termination of the ranges of Re covered for different values of β. In general, we observe that the interface velocity first decreases and then apparently stabilizes with increasing Re. This latter feature may be due to the fact that the separation point on the lee side of the cylinder tends to an asymptotic position.

For a given geometry of the cylinder array, simple dimensional considerations show that one must have a relation of the form

$$\frac{U_i}{U_*} = \frac{\lambda}{\sqrt{\kappa}} = f_1(\beta, Re, a/H) \to f(\beta, Re) \quad \text{as} \quad a/H \to 0, \tag{4.2}$$

where Re is the Reynolds number near the interface defined in (2.9). The nature of this Reynolds-number dependence at small Re may be inferred from the following argument (see Koch & Ladd 1997). After non-dimensionalizing lengths by $2a$, the velocity by U_* and the pressure gradient by $\mu U_*/4a^2$, the Navier–Stokes equations can be written as

$$\nabla \cdot \boldsymbol{u} = 0, \quad -\nabla p + \nabla^2 \boldsymbol{u} + \frac{8a^2}{H\sqrt{\kappa}} \boldsymbol{e}_x = Re\, \boldsymbol{u} \cdot \nabla \boldsymbol{u}\,. \tag{4.3}$$

Here the dimensionless imposed pressure gradient in the x direction has been written explicitly as $8a^2/(H\sqrt{\kappa})\boldsymbol{e}_x$. Upon expanding velocity and pressure in a regular perturbation series in Re

$$\boldsymbol{u} = \boldsymbol{u}_0 + Re\boldsymbol{u}_1 + Re^2\boldsymbol{u}_2 + \cdots, \quad \nabla p = \frac{8a^2}{H\sqrt{\kappa}} \boldsymbol{e}_x + \nabla p_0 + Re \nabla p_1 + Re^2 \nabla p_2 + \cdots \tag{4.4}$$

the leading-order velocity and pressure fields are found to satisfy the homogeneous Stokes equations while the higher-order fields contain inertial effects that depend on the lower-order fields:

$$-\nabla p_1 + \nabla^2 \boldsymbol{u}_1 = \boldsymbol{u}_0 \cdot \nabla \mathbf{u}_0\,, \tag{4.5}$$

$$-\nabla p_2 + \nabla^2 \boldsymbol{u}_2 = \mathbf{u}_0 \cdot \nabla \boldsymbol{u}_1 + \boldsymbol{u}_1 \cdot \nabla \boldsymbol{u}_0. \tag{4.6}$$

Since the Stokes equation is linear and the boundary conditions are periodic in x, the velocity field $\boldsymbol{u}_0$ is an even function of x. Thus, the right-hand side of (4.5) is odd in x and so is $\boldsymbol{u}_1$, which therefore makes no contribution to $U(y)$ defined in (3.6). For this reason, the $O(Re)$ contribution to the interface velocity vanishes and we find, at small Reynolds numbers,

$$\frac{\lambda}{\sqrt{\kappa}} = \lambda_0(\beta) + \lambda_2(\beta) Re^2. \tag{4.7}$$

This quadratic dependence is in agreement with the numerical result shown in figure 13(b) where the computed dimensionless slip velocity is plotted as a function of Re^2.

4.3. *Force and torque on the outermost layer of cylinders*

We now consider the hydrodynamic force, defined as

$$\boldsymbol{F} = \int_S \boldsymbol{\sigma} \cdot \boldsymbol{n}\, \mathrm{d}S - \pi a^2 \left(-\frac{\mathrm{d}p}{\mathrm{d}x} \boldsymbol{e}_x \right) \tag{4.8}$$

acting on the outermost cylinder layer. Here $\boldsymbol{\sigma}$ is the total fluid stress (i.e. pressure plus viscous) on the cylinder surface S and $\boldsymbol{n}$ is the outward unit normal. The second term $\pi a^2(-\mathrm{d}p/\mathrm{d}x)$ represents the 'effective buoyancy force' due to the applied pressure gradient and subtracting it from the total calculated force permits us to focus on the effect of the local flow around the bodies.

Figure 14 shows the horizontal (x-)component of $\boldsymbol{F}$, i.e. the drag force F_x, scaled by F_* defined in (2.10), which is proportional to the interfacial Reynolds number Re. The open and closed symbols are for $H/a = 17.1$ and 13.7, respectively, and the

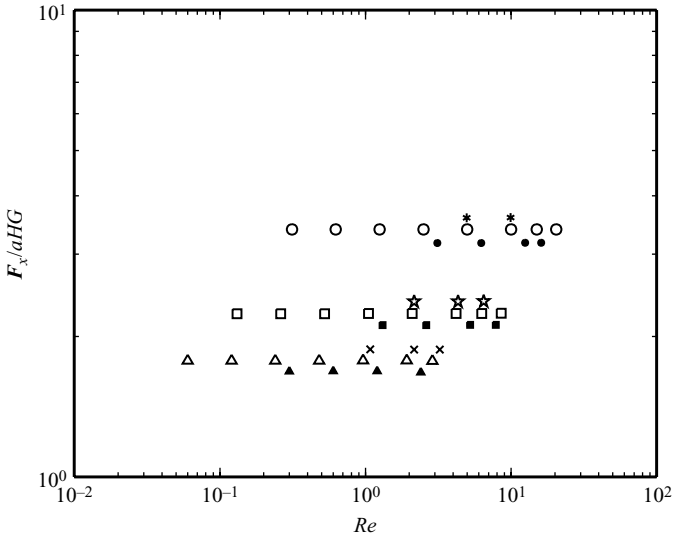

FIGURE 14. Non-dimensional drag force per unit length on the cylinders in the top layer with $G = -\mathrm{d}p/\mathrm{d}x$. The open and closed symbols are for $H/a = 17.1$ and 13.7, respectively, and the asterisks are for the staggered array with $H/a = 13.7$. Circles are for $\beta = 15\,\%$, squares for $\beta = 30\,\%$ and triangles for $\beta = 45\,\%$.

asterisks are for the staggered array with $H/a = 13.7$. Circles are for $\beta = 15\,\%$, squares for $\beta = 30\,\%$ and triangles for $\beta = 45\,\%$. Continuing the parity considerations made above, it is easy to show that the $O(Re)$ contribution to F_x vanishes leaving only an $O(Re)^2$ effect which is slightly negative, as evidenced by the slight downward bending of the data, and very small. The scaling by F_* removes part of the dependence on the channel width, but the difference between open and closed symbols indicates the presence of some residual dependence on the parameter a/H which, while small, does not appear to be quite negligible. The strongest dependence is on the volume fraction β to which F_x is seen to be approximately inversely proportional as suggested by (3.1).

Of greater interest is the lift force F_y, shown in figure 15 normalized by F_*; this force must vanish for $Re = 0$ due to the reversibility of inertia-less flow. Now the parity argument shows that F_y derives from the $O(Re)$ terms in the expansion (4.4) and is seen to grow rapidly with the interfacial Reynolds number Re until it appears to saturate at higher Re. The results exhibit very little sensitivity to volume fraction, channel height or array geometry, mostly depending on the Reynolds number. The saturation at the higher end of this variable (which implies a proportionality to the pressure gradient G by which F_y is scaled) is due to the fact that the flow pattern (e.g. the position of streamlines and stagnation points) tends to stabilize as Re increases. After this happens, since the spatial distribution of pressure and stress does not change any more, the force becomes only dependent on the levels of these quantities which, in a channel flow, are both proportional to the pressure gradient G.

We can get some insight into the mechanism causing this lift force by looking at the pressure and viscous stress distributions over the particle surface. Figures 16(a) and 17(a) are polar plots of the dimensionless pressure $(p - \tilde{p})/a(-\mathrm{d}p/\mathrm{d}x)$ and viscous stress $(\boldsymbol{\tau} \cdot \boldsymbol{n})/a(-\mathrm{d}p/\mathrm{d}x)$ around the topmost cylinders in the square array arrangement for 15 % and 45 %; $\tilde{p}$ is the surface average pressure and $\boldsymbol{n}$ the outward

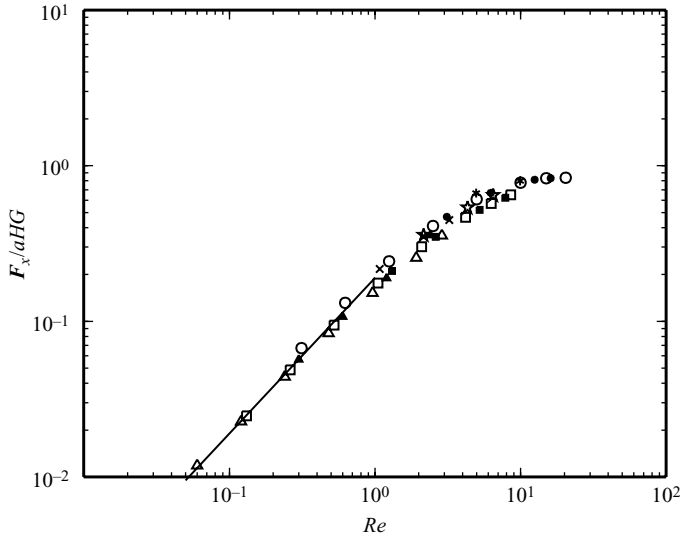

FIGURE 15. Non-dimensional lift force per unit length on the cylinders in the top layer with $G = -\mathrm{d}p/\mathrm{d}x$. The open and closed symbols are for $H/a = 17.1$ and 13.7, respectively, and the asterisks are for the staggered array with $H/a = 13.7$. Circles are for $\beta = 15\,\%$, squares for $\beta = 30\,\%$ and triangles for $\beta = 45\,\%$.

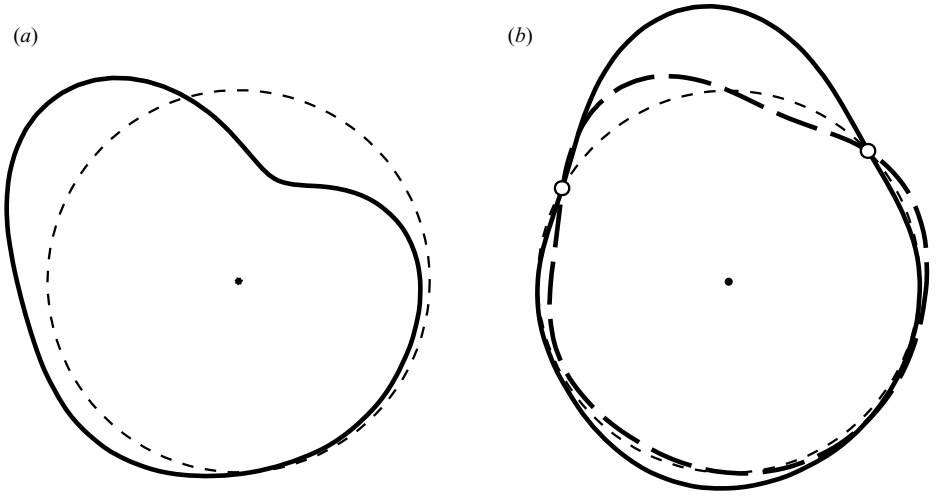

FIGURE 16. (*a*) The dimensionless pressure distribution over the surface of the topmost cylinders. The solid and dashed lines in (*b*) are the horizontal and vertical components of the viscous stress. The radius of the dashed circle is 30; the volume fraction is 15 %, the channel Reynolds number $Re_H = 420$, the interfacial Reynolds number $Re = 20.4$ and the channel width $H/a = 13.7$.

unit normal. The normal component of $\boldsymbol{\tau} \cdot \boldsymbol{n}$ vanishes by continuity and therefore both the x- and y-components vanish at the stagnation points mentioned earlier in connection with figure 10. The position of the pressure maxima and minima seen earlier in figure 10 clearly corresponds to these points. Even though the high-pressure region above the centre plane is comparable to the low pressure one, the latter is more concentrated towards the upper surface of the body, while the centre of the

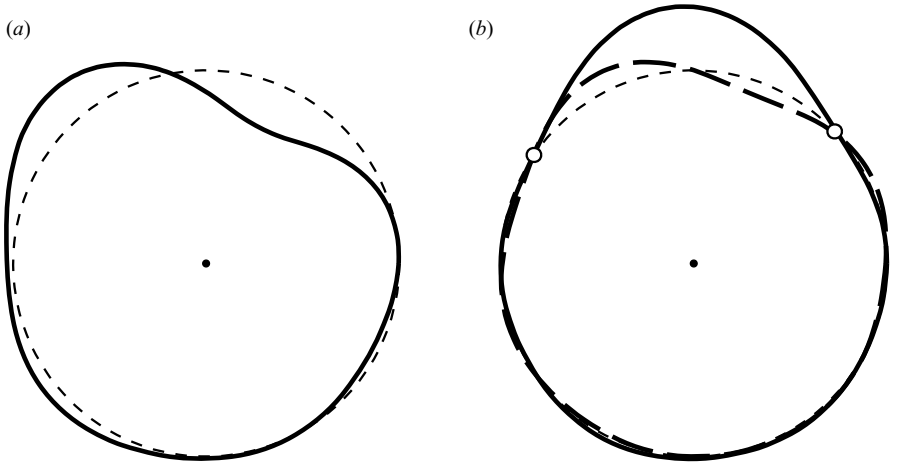

FIGURE 17. (*a*) The dimensionless pressure distribution over the surface of the topmost cylinder. The solid and dashed lines in (*b*) are the horizontal and vertical components of the viscous stress. The radius of the dashed circle is 30; the volume fraction is 45 %, the channel Reynolds number $Re_H = 308$, the interfacial Reynolds number $Re = 3.24$ and the channel height $H/a = 13.7$.

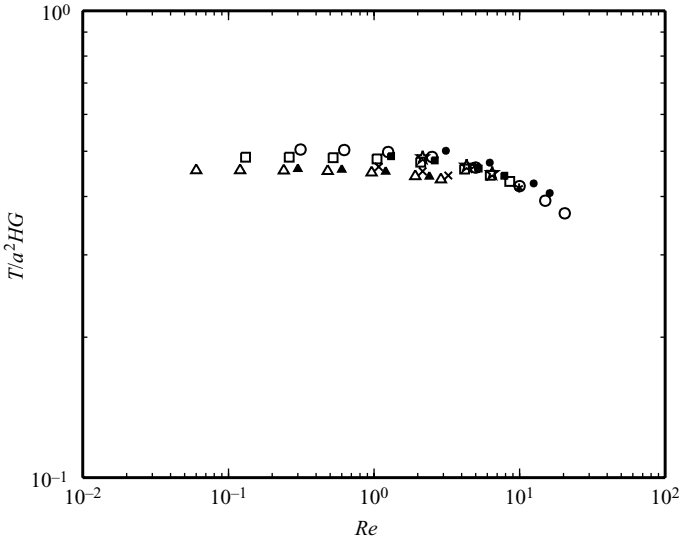

FIGURE 18. Non-dimensional couple per unit length on the cylinders in the top layer with $G = -\mathrm{d}p/\mathrm{d}x$. The open and closed symbols are for $H/a = 17.1$ and 13.7, respectively, and the asterisks are for the staggered array with $H/a = 13.7$. Circles are for $\beta = 15$ %, squares for $\beta = 30$ % and triangles for $\beta = 45$ %.

high pressure is displaced downward. The net result is therefore a 'suction' force away from the porous bed, aided by an upward pressure force on the underside of the particle (much decreased for $\beta = 45$ %). The figures show that the pressure effect is aided by the vertical component of the viscous stress (dashed lines).

Finally, figure 18 is the couple per unit length on the top cylinders normalized by L_* defined in (2.10). With this normalization the couple is approximately independent

of the interfacial Reynolds number up to $Re \sim 1$ (indicating that $L \propto -\mathrm{d}p/\mathrm{d}x$), and then slowly starts to decrease as the asymmetry between the tractions on the upper and lower sides of the cylinder, which is responsible for the couple, starts to decrease.

5. Conclusions

We have presented a numerical study of the two-dimensional flow past a regular array of cylinders partially obstructing a fluid flow as sketched in figure 1. Unlike most of the earlier studies, we have focused on the effects of fluid inertia on the various quantities which characterize the flow in the immediate vicinity of the porous medium interface: slip velocity, slip length and slip coefficient.

The most interesting conclusion of this work is the appearance of a lift force on the bodies at the surface of the porous medium only weakly dependent on the volume fraction and geometry of the array. This force vanishes at zero Reynolds number and increases nearly proportionally to it until it saturates at an approximately constant value for an interfacial Reynolds number greater than about 20. In this range the lift force per unit cylinder length is approximately

$$F_y \simeq 2a\tau_w \tag{5.1}$$

in which τ_w is of the order of the average shear stress at the surface of the porous medium. Our calculation of the drag force in the direction of the flow (figure 14) gives a somewhat larger result but of the same order. The couple per unit length acting on the topmost cylinder layer is about

$$T \simeq 2a^2\tau_w. \tag{5.2}$$

The numerical results for the square and staggered arrays are very close, which suggests a relative insensitivity to the detailed spatial arrangement of the bodies. This observation suggests that our results might hold with a reasonable quantitative accuracy also for random arrangements.

In the literature on sediment transport it is customary to make use of the so-called Shields number (see e.g. Ouriemi *et al.* 2007)

$$Sh = \frac{\tau_w}{(\rho_p - \rho)ga} \tag{5.3}$$

in which ρ_p and ρ are the particle and fluid density and g the acceleration of gravity. A critical value $Sh \sim 0.1$ is commonly used to characterize incipient sediment mobility. In principle one could imagine replacing τ_w by a combination of drag, lift and hydrodynamic couple which act in a direction favourable towards displacing the particle upward. Our results show that, numerically, this combination would be several times τ_w, so that the condition for incipient mobility would move closer to the weight of the particles as one would expect. The lift force may also play a role in destabilizing particle layers dominated by horizontal force chains. Clearly, these matters need to be investigated further with more realistic sediment models.

This study was supported by National Science Foundation under grants CBET-0625138 and CBET-0754344.

REFERENCES

Adler, P. M., Mills, P. M. & Quemada, D. C. 1978 Application of a self-consistent model to permeability of a fixed swarm of permeable spheres. *A.I.Ch.E. J.* **24**, 354–357.

Agelinchaab, M., Tachie, M. & Ruth, D. 2006 Velocity measurement of flow through a model three-dimensional porous medium. *Phys. Fluids* **18**, 017105.

Beavers, G. S. & Joseph, D. D. 1967 Boundary conditions at a naturally permeable wall. *J. Fluid Mech.* **30**, 197–207.

Brinkman, H. 1947 A calculation of the viscous force exerted by a flowing fluid on a dense swarm of particles. *Appl. Sci. Res.* A**1**, 27–34.

Choi, H. G., & Joseph, D. D. 2001 Fluidization by lift of 300 circular particles in plane Poiseuille flow by direct numerical simulation. *J. Fluid Mech.* **438**, 101–128.

Goharzadeh, A., Khalili, A. & Jørgensen, B. B. 2005 Transition layer thickness at a fluid-porous interface. *Phys. Fluids* **17**, 057102.

Hill, R., Koch, D. & Ladd, A. 2001 Moderate-Reynolds-number flows in ordered and random arrays of spheres. *J. Fluid Mech.* **448**, 243–278.

Hou, S., Zou, Q., Chen, S., Doolen, G. & Cogley, A. 1995 Simulation of cavity flow by the lattice Boltzmann method. *J. Comp. Phys.* **118**, 329–347.

James, D. & Davis, A. 2001 Flow at the interface of a fibrous porous medium. *J. Fluid Mech.* **426**, 47–72.

Koch, D. & Ladd, A. 1997 Moderate Reynolds number flow through periodic and random arrays of aligned cylinders. *J. Fluid Mech.* **349**, 31–66.

Koplik, J., Levine, H. & Zee, A. 1983 Viscosity renormalization in the Brinkman equation. *Phys. Fluids* **26**, 2864–2870.

Larson, R. & Higdon, J. 1986 Microscopic flow near the surface of a two-dimensional porous medium. Part 1. Axial flow. *J. Fluid Mech.* **166**, 449–472.

Larson, R. E. & Higdon, J. J. L. 1987 Microscopic flow near the surface of two-dimensional porous media. Part 2. Transverse flow. *J. Fluid Mech.* **178**, 119–136.

Le Bars, M. & Worster, M. G. 2006 Interfacial conditions between a pure fluid and a porous medium: implications for binary alloy solidification. *J. Fluid Mech.* **550**, 149–173.

Martys, N., Bentz, D. & Garboczi, E. 1994 Computer simulation study of the effective viscosity in Brinkman's equation. *Phys. Fluids* **6**, 1434–1439.

Ouriemi, M., Aussillous, P., Medale, M., Peysson, Y. & Guazzelli, E. 2007 Determination of the critical Shields number for particle erosion in laminar flow. *Phys. Fluids* **19**, 061706.

Patil, D. V., Lakshmisha, K. N. & Rogg, B. 2006 Lattice Boltzmann simulation of lid-driven flow in deep cavities. *Comput. Fluids* **35**, 1116–1125.

Pozrikidis, C. 2001 Shear flow over a particulate or fibrous plate. *J. Engng Math.* **39**, 3–24.

Sahraoui, M. & Kaviany, M. 1992 Slip and no-slip velocity boundary conditions at interface of porous, plain media. *Intl J. Heat Mass Transfer* **35**, 927–943.

Sangani, A. & Acrivos, A. 1982 Slow flow through a periodic array of spheres. *Intl J. Multiphase Flow* **8**, 343–360.

Sangani, A. & Behl, S. 1989 The planar singular solutions of Stokes and Laplace equations and their application to transport processes near porous surfaces. *Phys. Fluids* A**1**, 21–37.

Sangani, A. & Yao, C. 1988 Transport properties in random arrays of cylinders. II. Viscous flow. *Phys. Fluids* **31**, 2435–2444.

Shen, C. & Floryan, J. M. 1985 Low Reynolds number flow over cavities. *Phys. Fluids* **28**, 3191–3202.

Smith, S. H. 1987 Stokes flow past slits and holes. *Intl J. Multiphase Flow* **13**, 219–231.

Tachie, M., James, D. & Currie, D. 2003 Velocity measurement of a shear flow penetrating a porous medium. *J. Fluid Mech.* **493**, 319–343.

Tachie, M., James, D. & Currie, I. 2004 Slow flow through a brush. *Phys. Fluids* **16**, 445–451.

Takagi, S., Oğuz, H., Zhang, Z. & Prosperetti, A. 2003 PHYSALIS: a new method particle simulation. Part II. Two-dimensional Navier–Stokes flow around cylinders. *J. Comput. Phys.* **187**, 371–390.

Zhang, Z. Z. & Prosperetti, A. 2003 A method for particle simulation. *J. Appl. Mech.* **70**, 64–74.

Zhang, Z. & Prosperetti, A. 2005 A second-order method for three-dimensional particle flow simulations. *J. Comput. Phys.* **210**, 292–324.